Article

Not peer-reviewed version

Application of Symmetric Neural Networks for Bead Geometry Determination in Wire and Arc Additive Manufacturing (WAAM)

Aitor Fernández-Zabalza , Fernando Veiga * , Alfredo Suárez , Virginia Uralde , Xabier Sandua , and José Ramón Alfaro

Posted Date: 3 January 2025

doi: 10.20944/preprints202501.0027.v1

Keywords: Weld Bead Geometry Prediction; Machine Learning in Additive Manufacturing; Process Parameter Optimization in arc-DED

 doi:10.20944/preprints202501.0027.v1

Article

Application of Symmetric Neural Networks for Bead Geometry Determination in Wire and Arc Additive Manufacturing (WAAM)

Aitor Fernández-Zabalza [1], Fernando Veiga [1,*], Alfredo Suárez [2], Virginia Uralde [1], Xabier Sandua [1] and José Ramón Alfaro [1]

[1] Department of Engineering, Public University of Navarre, Los Pinos Building, Campus Arrosadía, 31006 Pamplona, Navarra, Spain

[2] TECNALIA, Basque Research and Technology Alliance (BRTA), Parque Científico, Parque Científico y Tecnológico de Gipuzkoa, E20009 Donostia-San Sebastián, Spain

* Correspondence: fernando.veiga@unavarra.es

Abstract: Accurate prediction of weld bead geometry is crucial for ensuring the quality and consistency of Wire and Arc Additive Manufacturing (WAAM), a specific form of Directed Energy Deposition (DED) that utilizes arc welding. Despite advancements in process control, predicting the shape and dimensions of weld beads remains challenging due to the complex interactions between process parameters and material behavior. This paper addresses this challenge by exploring the application of symmetrical neural networks to enhance the accuracy and reliability of geometric predictions in WAAM. By leveraging advanced machine learning techniques and incorporating the inherent symmetry of the welding process, the proposed models aim to precisely forecast weld bead geometry. The use of neuronal networks and experimental validation demonstrate the potential of symmetrical neural networks to improve prediction precision, contributing to more consistent and optimized WAAM outcomes.

Keywords: weld bead geometry prediction; machine learning in additive manufacturing; process parameter optimization in arc-DED

1. Introduction

In recent years, wire arc additive manufacturing (WAAM), a variant of directed energy deposition (DED) technology, has emerged as a key area of focus in the field of additive manufacturing [1–3]. WAAM has attracted significant attention due to its ability to manufacture medium to large-scale metal components at high deposition rates, offering a cost-effective solution for industries such as aerospace, automotive and energy [4]. Unlike other additive manufacturing techniques, WAAM uses an electric arc to melt metal wire and deposit it layer by layer, enabling the creation of medium complexity geometries and some lightweight designs [5]. The robust deposition rates and flexibility of this technology have positioned it as a promising alternative to traditional manufacturing methods, particularly for producing medium to large structural components [6]. However, the successful application of WAAM depends on the precise control of several parameters that influence the quality of the final product, which makes ongoing research in this area critical [7,8].

The rapid adoption of WAAM is largely attributed to its numerous advantages over traditional additive and other manufacturing processes [9]. WAAM's ability to build elements by layer by layer methodology with relatively low material waste, coupled with the potential for large build volumes, makes it an attractive option for producing components that would be prohibitively expensive or difficult to manufacture using conventional techniques [10]. In addition, the lower raw material cost of wire compared to metal powders used in powder bed fusion (PBF) methods, coupled with WAAM's higher deposition rates, further enhance its attractiveness [6,11]. Despite these advantages,

 doi:10.20944/preprints202501.0027.v1

the success of the process depends on careful selection and control of parameters such as wire feed rate, travel speed, arc voltage and substrate plate thickness [12,13].

One of the critical factors influencing the quality of components produced by WAAM is the thickness of the substrate plate, which serves as the base on which the layers of material are deposited [10,12]. Substrate thickness plays a significant role in determining the heat dissipation characteristics during the welding process, directly impacting the weld penetration, bead geometry, and overall structural integrity of the final component. Thicker substrates generally offer better heat dissipation, reducing the risk of excessive heat buildup, which can lead to defects such as warping, distortion, or poor fusion between layers. Conversely, thinner substrates may not dissipate heat as effectively, potentially leading to overheating, increased residual stresses, and a higher likelihood of defects [14,15].

The interaction between the heat generated by the electric arc and the substrate is complex and highly dependent on the thermal properties of the materials involved [16]. The substrate's ability to absorb and dissipate heat affects the cooling rate of the deposited material, which in turn influences the microstructure and mechanical properties of the final part [17,18]. For instance, rapid cooling on a thinner substrate might lead to a finer microstructure, while slower cooling on a thicker substrate could result in a coarser grain structure. These microstructural differences can significantly impact the produced components performance, particularly in applications where high strength, toughness, and fatigue resistance are required [19]. Therefore, understanding and optimizing the interplay between substrate thickness and other process parameters is crucial for achieving the desired mechanical properties and ensuring the reliability of WAAM-fabricated components [6].

Achieving consistent bead geometry is one of the most significant challenges in WAAM, as the geometry directly affects the structural integrity and dimensional accuracy of the final element [20]. Bead geometry refers to the shape and size of the weld bead deposited in each pass, including its width, height and penetration depth [5,21]. The geometry of the initial beads is particularly important, as it sets the foundation for subsequent layers and ultimately determines the quality of the finished component[22]. Traditional approaches to controlling bead geometry in WAAM have typically focused on maintaining a constant transverse bead shape during deposition. However, these approaches often overlook the longitudinal variations that can occur, especially when there are changes in the substrate thickness or other process conditions.

In real applications, the longitudinal bead geometry may vary due to several factors, including fluctuations in heat input, variations in wire feed speed, and changes in the substrate's thermal properties [11]. These variations can lead to inconsistencies in layer thickness, poor fusion between layers, and deviations from the desired part dimensions. Moreover, the cumulative effect of small variations in bead geometry can result in significant defects, such as voids, cracks, or uneven surfaces, which can compromise the element's structural integrity[23]. Addressing these challenges requires a deeper understanding of the factors that influence bead geometry and the development of advanced control strategies that can adapt to changes in process conditions in real-time [14,24].

To overcome the challenges associated with bead geometry control in WAAM, researchers have increasingly turned to advanced process monitoring and control techniques [25]. One promising approach involves the integration of real-time monitoring systems with machine learning algorithms to predict and optimize bead geometry during the manufacturing process [26]. These systems typically employ a combination of sensors, such as infrared cameras, laser profilometers, and pyrometers, to capture real-time data on the weld pool's temperature, shape, and size [7,12,27,28]. By analyzing this data, machine learning models can predict the resulting bead geometry and make real-time adjustments to process parameters, such as wire feed speed, travel speed, and arc voltage, to maintain consistent bead quality [13,15].

In addition to real-time monitoring, neural networks have shown great potential in predicting bead geometry based on a set of input parameters, including welding conditions and substrate characteristics [24,29]. These networks can be trained using data from previous WAAM processes to learn the relationships between input variables and bead geometry outcomes [2]. Once trained, the

 doi:10.20944/preprints202501.0027.v1

neural network can predict the optimal set of process parameters for a given substrate thickness and desired bead geometry, helping to reduce trial-and-error in parameter selection and improving the overall efficiency of the manufacturing process. Furthermore, neural networks can adapt to changes in process conditions, making them particularly valuable for complex geometries or varying substrate thicknesses, where traditional control methods may struggle to maintain consistent bead quality.

The advancements in artificial intelligence, particularly the application of neural networks in WAAM, have significant implications for the industry. Neural networks are increasingly being utilized to model and optimize the complex relationships between process parameters and output quality, providing insights that are difficult to obtain through traditional methods. In WAAM, neural networks can predict not only bead geometry but also potential defects, material properties, and overall build quality, allowing for real-time adjustments that enhance the manufacturing process.

One key application of neural networks in WAAM is in the prediction and control of thermal cycles during the deposition process. The thermal history of the weld pool and surrounding material greatly influences the microstructure and mechanical properties of the final part. By training neural networks on thermal data from previous builds, manufacturers can predict the thermal behavior under various process conditions and adjust parameters to ensure optimal cooling rates, minimizing the risk of defects like cracking or porosity. This capability is particularly valuable in producing components from high-strength alloys, where precise thermal management is critical to achieve the desired material properties.

Another important application is in the real-time monitoring and correction of bead geometry. Neural networks can analyze sensor data to detect deviations from the desired bead shape and adjust process parameters instantaneously, ensuring consistent layer quality and reducing the likelihood of defects accumulating over multiple layers [23]. This real-time feedback loop is essential in maintaining the dimensional accuracy and structural integrity of complex parts, especially in industries where precision is paramount, such as aerospace [30].

Moreover, neural networks can be used to optimize the entire WAAM process, from initial parameter selection to final part inspection [13,24]. By integrating neural networks with other AI technologies, such as genetic algorithms or reinforcement learning, manufacturers can explore a vast design space and identify optimal process parameters for specific materials and geometries. This holistic approach not only improves the efficiency of the manufacturing process but also enhances the performance and reliability of the final product [31].

The future of WAAM lies in the continued integration of artificial intelligence, particularly neural networks, into the manufacturing process. As AI technologies evolve, they will enable more sophisticated predictive models and adaptive control systems that can respond to real-time data with greater accuracy and precision. Research into neural network architectures and training methods will further enhance their ability to model complex relationships in WAAM, leading to improved process control and components quality [26].

2. Materials and Methods

This section describes the hardware elements, the auxiliary elements and the communication between the different systems that make up the solution.

2.1. Experimental Set-Up

The Addilan (Durango, Spain) WAAM machine was utilized to manufacture two walls. This machine features a tilt table with an additional 2-axis capability and operates within a closed chamber filled with an inert atmosphere, making it well-suited for processing reactive materials like titanium or aluminum. While primarily employing the GMAW process, the machine is also capable of supporting other welding processes, including GTAW and PAW.

In the GMAW process, an electric arc is generated between the wire and the workpiece, causing the material to melt and subsequently be deposited layer by layer onto the substrate to form the wall.

 doi:10.20944/preprints202501.0027.v1

The machine offers a build envelope of 1300 × 900 × 500 mm, with a maximum load capacity of 300 kg.

The additive manufacturing setup included an MIG/MAG welding power source, specifically the Titan XQ 400 AC puls, and a wire feeder (M drive 4 Rob5 XR RE), both supplied by the welding equipment manufacturer EWM (Mündersbach, Germany). To monitor the geometry of the deposited layers and assess the cooling time between layers, an Optris (Berlin, Germany) compact pyrometer and a QuellTech (Munich, Germany) Q4 laser scanner were mounted on the welding torch holder.

A personal computer was employed to manage and monitor welding parameters throughout the process, with data being sent to a remote database for easy access.

The wire used in the GMAW process to fabricate the walls, applying both overlapping and oscillating techniques, was ER70S-6 mild steel (DIN 8559SG2). According to the supplier, Table 1 shows composition of the wire and substrate. The wire diameter used for direct energy deposition was 1.2 mm.

The substrate plate employed was S235JR steel (DIN ST37-2) in sheet form, available in multiple thicknesses. S235JR is a structural carbon steel commonly used in construction and engineering, conforming to the EN 10025-2 standard. Its typical composition includes up to 1.50% Mn, 0.17% Si, 0.20% C, and trace amounts of other elements like P and S, with the majority of the material being Fe.

Table 1. Composition of the wire (ER70S-6) and substrate (SS235JR) materials.

Material	Mn	Si	C	Cr	Cu	Ni	S	P	Mo	Ti	Zr	Fe
ER70S-6	1.64	0.94	0.06	0.02	0.02	0.02	0.016	0.013	0.005	0.004	0.002	Balance
S235JR	1.5	0.17	0.2	0.02	0.2	0.01	0.045	0.045	-	-	-	Balance

2.2. Test Parameters for Process Characterization

Table 2 presents detailed welding parameters for three test plates labeled as Sheet 1, Sheet 2, and Sheet 3. Each plate undergoes nine welding passes, with parameters such as substrate thickness, wire feed speed, deposition rate, and travel speed being adjusted across these passes. The substrate material used throughout the tests is S235JR steel, with a density of 7850 kg/m^3, and the filler material is ER70S-6. Substrate thickness varies among the plates: 8 mm for Sheet 1, 10 mm for Sheet 2, and 30 mm for Sheet 3. Other parameters, including gas composition (20% CO2 and 80% Ar), gas flow rate (17 L/min), nozzle diameter (20 mm), wire diameter (1.2 mm), and welding process (MIG/MAG PULS), remain constant across all tests.

The tests aim to vary the wire feed speed, deposition rate, and travel speed while maintaining the other conditions. Wire feed speeds range from 5 m/min to 15 m/min, resulting in deposition rates between 2.66 kg/h and 8 kg/h. The travel speed varies from 50 cm/min to 150 cm/min. This systematic variation across the welding passes provides a robust dataset to evaluate how different welding parameters influence the quality and characteristics of the welds on each plate.

Table 2. Process parameters for the geometry characterization.

Test	Sheet	Substrate Thickness (mm)	Wire Feed Speed (m/min)	Deposition Rate (kg/h)	Travel Speed (cm/min)
1	Sheet 1	8	5	2.66	50
2	Sheet 1	8	10	5.33	100
3	Sheet 1	8	15	8	150
4	Sheet 2	10	5	2.66	50
5	Sheet 2	10	10	5.33	100
6	Sheet 2	10	15	8	150
7	Sheet 3	30	5	2.66	50

 doi:10.20944/preprints202501.0027.v1

8	Sheet 3	30	10	5.33	100
9	Sheet 3	30	15	8	150

3. Results

This section presents a comprehensive analysis of bead geometry and its influencing factors. It explores the geometric characteristics of beads under various conditions, the impact of plate thickness on these parameters, and the application of symmetric neural networks for accurate bead geometry estimation.

In the first subsection, the bead geometry, including its width, height, and cross-sectional area, is analyzed to establish baseline trends and identify key factors affecting uniformity and quality.

Then the effect of plate thickness on bead geometry is investigated, how varying plate thickness influences bead geometry, revealing its critical role in achieving consistent and stable outcomes.

The final subsection discusses the use of symmetric neural networks to estimate bead geometry, highlighting the model's accuracy and its potential for process optimization.

3.1. Analysis of Bead Geometry

To analyze bead geometry, a macroscopic image of a cross-sectional view of the bead was selected, as shown in Figure 1a. This image provides detailed information about geometric characteristics, such as width, height, and cross-sectional area. Focusing on a single cross-sectional plane allows an accurate assessment of the bead's shape precisely, as well as the identification of deviations or irregularities influenced by process parameters or material properties. This approach ensures a precise evaluation of the bead geometry, forming the basis for further analysis and comparison.

The selected indicators, as shown in Figure 1c, represent various geometric characteristics of the bead:

- h_0, h_1, h_2: These are vertical measurements corresponding to the bead's height. h_0 indicates the maximum height from the baseline, while h_1 and h_2 represent additional height measurements at specified lateral positions to assess the bead's shape.
- w_0, w_1, w_2**:** These are horizontal measurements of the bead's width. w_0 represents the total width of the bead, while w_1 and w_2 capture intermediate widths at different height levels in order to analyze the contour profile, as shown in Figure 1b.
- HAZ (Heat-Affected Zone): This region indicates the area of material affected by heat during the process, providing critical information about thermal diffusion and material properties. It is highlighted in red in Figure 1c.
- Penetration: This measurement reflects the depth of material fusion or interaction with the substrate, crucial for evaluating joint quality and strength, as shown in Figure 1c. It is represented by the green area below the bead.

These indicators provide a detailed representation of the bead geometry and thermal effects, essential for analyzing the process and ensuring optimal results.

 doi:10.20944/preprints202501.0027.v1

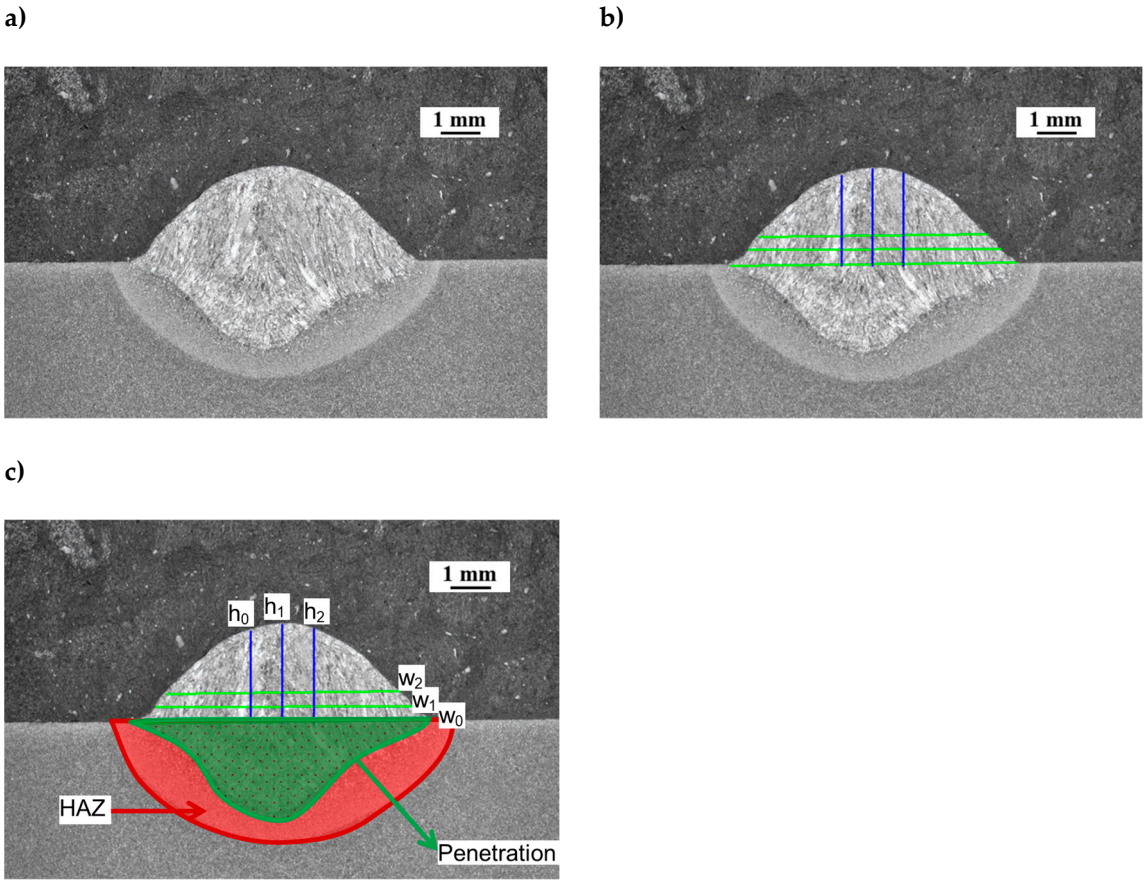

Figure 1. Macroscopic images of the bead cross-section: (a) bead geometry without annotations, (b) bead geometry with selected measurement indicators, including height (h_0, h_1, h_2) and width (w_0, w_1, w_2), and (c) detailed representation of the Heat-Affected Zone (HAZ) and penetration area.

Table 3 presents the geometric data of the bead for the performed tests, corresponding to the same tests previously presented in Table 2. Each test is numbered sequentially from 1 to 9. The lengths w_1, w_2 and w_3 represent three different width measurements taken at different points of the welded material, as it is described in Figure 1c. Likewise h_1, h_2 and h_3 parameters, represent three different height measurements. In addition, the area of the heat affected zone (HAZ) indicates the region of the material that has been affected by heat due to welding process. The penetration parameter measures the depth of penetration of heat or material flow. Finally, the surface area is considered the total area of the cross-section protruding to the substrate sheet. The data represents the measurements that capture various geometric dimensions (widths and heights) and areas (HAZ, penetration, and total area) for the different test conditions.

Table 3. Geometry of the bead in the different performed test.

Test	w_1 (mm)	w_2 (mm)	w_3 (mm)	h_1 (mm)	h_2 (mm)	h_3 (mm)	HAZ (mm^2)	Penetration (mm^2)	Area (mm^2)
1	7.10	6.22	5.48	2.15	2.37	2.33	17.48	8.65	10.62
2	7.00	5.77	4.95	2.52	2.67	2.48	21.59	12.46	11.65
3	7.10	5.25	4.82	2.65	2.80	2.72	24.41	15.83	11.87
4	6.75	5.80	5.22	2.10	2.33	2.18	16.63	8.34	9.63
5	7.17	6.47	5.65	2.17	2.32	2.23	22.68	12.87	10.46
6	7.33	5.82	5.30	2.38	2.52	2.37	26.67	17.10	10.90

 doi:10.20944/preprints202501.0027.v1

7	8.20	7.08	5.83	1.83	1.98	1.88	19.96	9.49	9.51
8	8.45	7.32	6.10	1.95	2.10	2.02	23.94	13.01	10.48
9	7.42	5.63	5.05	2.40	2.52	2.43	25.44	17.29	10.53

3.2. Effect of Plate Thickness and Deposition Rate on Bead Geometry

In this section the Response Surface Methodology (RSM) is used for analyzing the evolution of outputs as a function of input variables, as it allows for efficient modeling and understanding of the relationship between independent variables (such as substrate thickness and deposition rate) and responses (such as weld bead area, heat-affected zone (HAZ), and penetration), as shown in Figure 2. RSM helps to identify interactions between factors and provides a clear graphical representation of how these affect welding process properties. Additionally, by simplifying the system through mathematical functions, it enables the optimization of operational parameters to achieve the desired results, thus improving process accuracy and reducing the need for costly and time-consuming experiments. This makes RSM an invaluable tool in the analysis and continuous improvement of industrial processes. The generated response surfaces provide a comprehensive view of how substrate thickness and deposition rate influence various aspects of the welding process, particularly the welding bead area (Area) in Figure 2a, heat-affected zone (HAZ) in Figure 2b, and penetration in Figure 2c.

As substrate thickness increases, the heat-affected zone (HAZ) also tends to enlarge. This is because a thicker substrate absorbs more heat, causing the heat to spread over a larger area. The effect is even more pronounced when the deposition rate is increased, as higher deposition rates introduce more heat into the material. The combination of these two factors—greater substrate thickness and higher deposition rate—results in a significant expansion of the HAZ area. This relationship highlights how the interaction between heat input and material characteristics influences the extent of thermal effects during welding.

Regarding penetration, the effect of substrate thickness is more complex. For thinner substrates, penetration increases significantly with higher deposition rates. This is because a thinner substrate requires less heat to reach the necessary depth for penetration. However, as the substrate thickness increases, the penetration rate starts to plateau or even decrease slightly, especially at higher deposition rates. The thicker substrate absorbs more heat, which reduces the intensity of heat transfer into the material, leading to less deep penetration. Thus, penetration is more sensitive to changes in deposition rate when the substrate is thin, but this effect diminishes as the substrate thickens.

When considering the overall area of the welding bead, both substrate thickness and deposition rate contribute to an increase in the bead area. Thicker substrates allow for a larger welding area because they absorb more heat, leading to a wider spread of the molten material. However, the deposition rate plays a more dominant role in increasing the bead area. As the deposition rate increases, more filler material is deposited, resulting in a thicker and wider bead. This effect is consistent across the tested range of deposition rates, where the bead area grows almost linearly with deposition rate, suggesting that the amount of filler material directly influences the bead's size.

 doi:10.20944/preprints202501.0027.v1

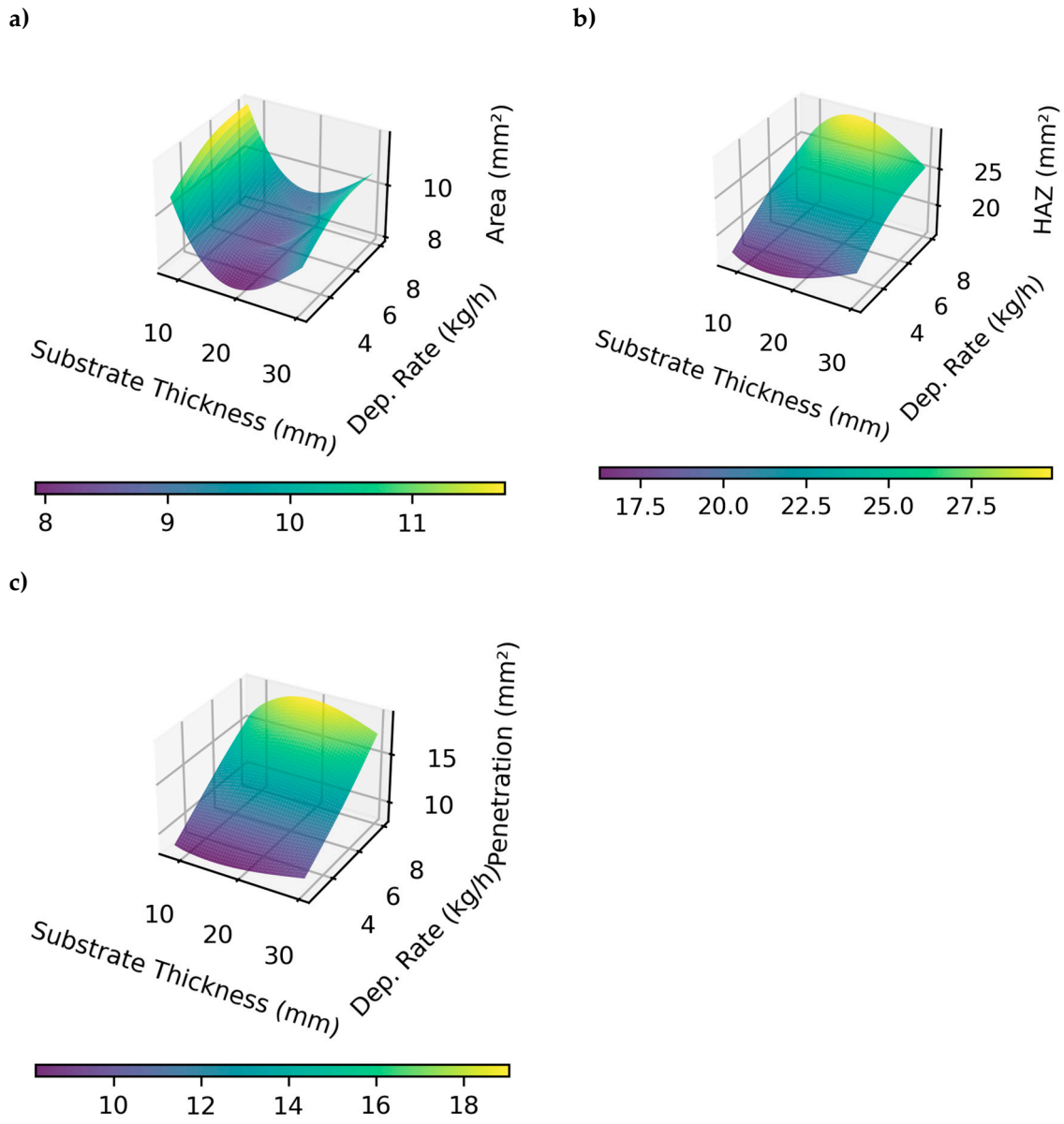

Figure 2. RSM of the bead cross-section areas: a) Bead Area over the substrate, b) HAZ, and c) Penetration area.

In summary, the deposition rate emerges as the key factor influencing the size of the HAZ, penetration, and bead area. It has a strong positive correlation with all three areas, making it the primary variable in determining the weld's thermal and mechanical properties. On the other hand, substrate thickness has a more nuanced effect. While it increases the HAZ and bead area, it can reduce penetration at higher thicknesses due to increased heat dissipation. Understanding the interplay between substrate thickness and deposition rate is essential for optimizing welding parameters to achieve desired results, balancing thermal and mechanical performance in the weld zone.

The analysis focuses on identifying potential correlations between the areas of interest in the weld bead and measurable parameters during the welding process. Specifically, the heights and widths of the bead, which can be accurately obtained using a profilometer, are considered alongside the voltage and current signals generated by the welding equipment. These parameters are critical as they provide valuable insights into the welding process and its influence on the resulting weld geometry, offering opportunities to optimize and control the process for improved quality and consistency. The results reveal that weld bead areas exhibit a strong positive correlation with the bead widths (w_1, w_2, w_3) indicating that the width of the bead is a critical factor influencing the size

 doi:10.20944/preprints202501.0027.v1

of the affected areas. Heights (h_1, h_2, h_3) show a moderate correlation with the weld areas, suggesting that vertical dimensions also play a role, albeit to a lesser extent than widths, as it can be seen in Figure 3.

Voltage (V) and current (I) display varying degrees of correlation with the areas, reflecting their influence on energy input and material deposition during welding. Higher values of these parameters generally correspond to larger weld areas. Furthermore, substrate thickness and deposition rate, while exhibiting some correlation with the areas, are identified as secondary contributors to the geometry of the bead. The findings are summarized visually through a correlation matrix heatmap, where the color intensity highlights the strength and direction of the relationships, providing a comprehensive understanding of the factors that affect weld bead areas.

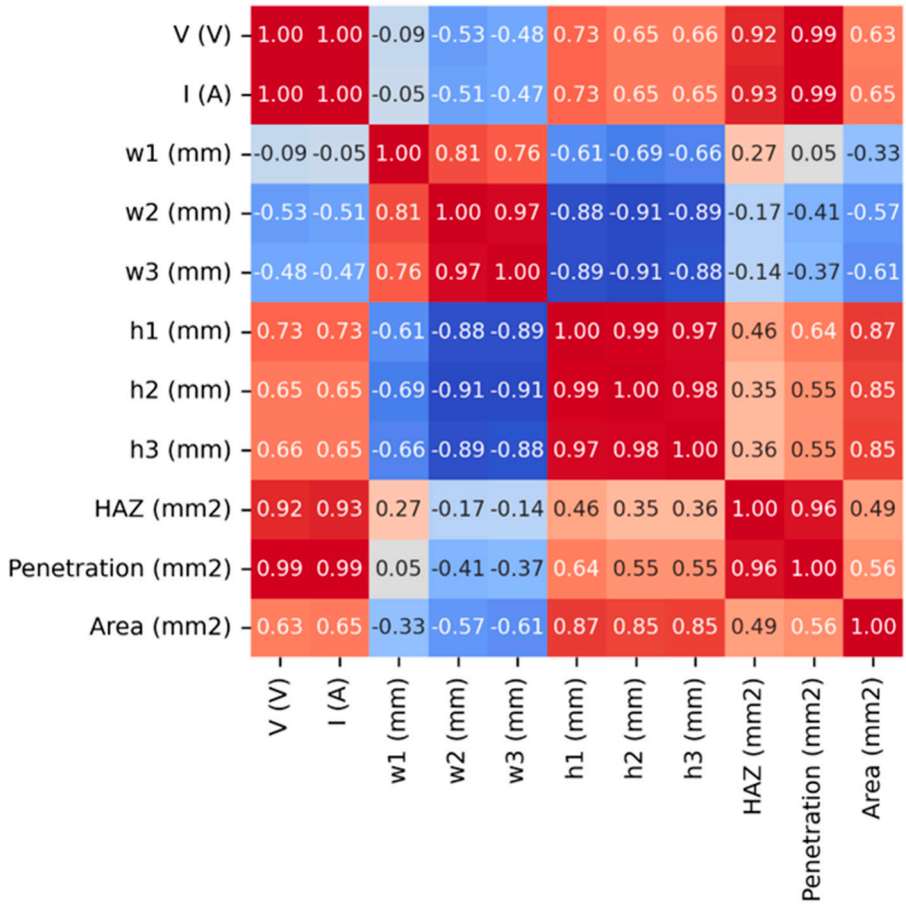

Figure 3. Correlation matrix heatmap.

3.3. Bead Geometry Estimation by Means of Symmetric Neural Networks

The process to generate the Figure 4 involves developing an algorithm designed to analyze a profile, identifying its most prominent peak (corresponding to the bead), and compute key geometric features associated with it. The steps are described below. Initially, a dataset representing a profile was provided, consisting of an independent variable x (horizontal axis) and a dependent variable z (vertical axis). A specific region of interest within the profile, referred as the "Manual Zone," was manually selected, defined by a range of x-values. This region was chosen to include the bead in the whole profile.

The algorithm first filtered the data to isolate the values within the Manual Zone. A detrending process was then applied to the z-values, removing any linear trend from the data to highlight local variations more effectively. From this adjusted signal, the algorithm identified the index

 doi:10.20944/preprints202501.0027.v1

corresponding to the maximum value, representing the bead within the Manual Zone. This region became the focus of further analysis.

To analyze the bead's geometry, thresholds relative to its maximum height were defined. For each threshold, the algorithm located the closest points on the left and right of the maximum value where the adjusted signal dropped below the threshold. These crossing points were used to determine the width of the bead at various heights. Specifically, the width was calculated as the horizontal distance between the left and right crossing points for each threshold. The absolute height of the bead was also recorded.

The results were visualized in a two-panel Figure 4. The left panel displays the original profile with the Manual Zone highlighted. The right panel shows the detrended profile, focusing on the bead. Horizontal lines at different threshold levels and vertical lines connecting the crossing points to the x-axis were drawn, illustrating the computed widths. This visualization provides a clear representation of the bead's geometric characteristics, including its maximum height and widths at different levels.

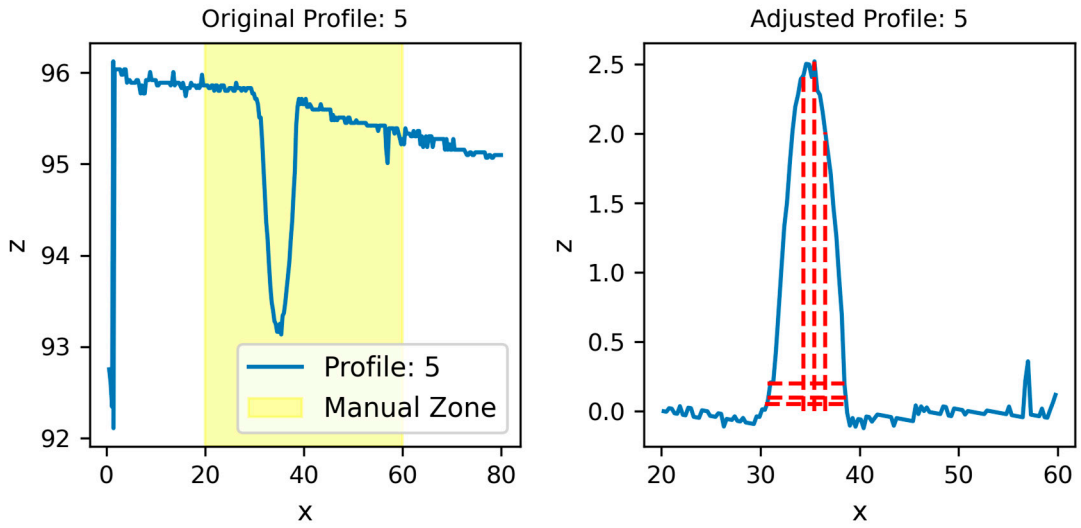

Figure 4. Weld bead profile measured raw by profilometer and then treated to extract characteristic heights and widths in profile 5 of Test 7.

The neural network designed for this task is built with a symmetrical structure, a characteristic often preferred for regression problems like predicting areas (penetration, bead's area and HAZ). This symmetry is evident in the architecture, where the number of neurons decreases progressively with each layer. The design mimics the shape of a funnel, which enables the network to condense the input information effectively while simplifying the data as it moves deeper into the layers. Starting with a larger number of neurons in the first hidden layer and gradually reducing this count allows the network to extract features hierarchically, ensuring that important patterns are retained while noise is filtered out.

To further enhance the learning process, Rectified Linear Unit (ReLU) activation functions are applied across the hidden layers. ReLU is computationally efficient and introduces non-linearity, which is crucial for modeling complex relationships between the input features and the target variables. At the output layer, the model employs a linear activation function, ensuring that the predictions are not constrained and remain suitable for continuous target variables like the Areas.

The network is also designed with considerations for generalization and optimization. Regularization techniques, if applied, would ensure that no single layer dominates, maintaining a balanced and uniform approach to learning. Additionally, the Adam optimizer helps adjust the learning rates dynamically for each parameter, promoting a smooth and efficient convergence.

 doi:10.20944/preprints202501.0027.v1

Looking at the training results, the graphs for loss and MAE (Mean Absolute Error) provide a clear view of the learning dynamics. The training loss exhibits a rapid decline during the initial epochs, Figure 5a, demonstrating how quickly the model learns the patterns in the training data. The validation loss follows a similar trend but stabilizes at a slightly higher value, which indicates the presence of a generalization gap. However, both losses asymptotically approach stable values after approximately 50 epochs, signaling that the model has converged and is no longer overfitting or underfitting.

The MAE graph, Figure 5b, similarly reflects steady improvement in prediction accuracy for both the training and validation sets. The gradual stabilization of the validation MAE highlights the model's ability to make consistently better predictions, ultimately reaching an asymptote that suggests effective learning.

Overall, this neural network's symmetrical design ensures a balanced and robust approach to processing input features. By maintaining a structured reduction in complexity and utilizing appropriate activations, the model effectively captures the underlying patterns in the data. The convergence of both loss and MAE to stable values further reinforces that the network has successfully learned without overfitting, making it well-suited for predicting

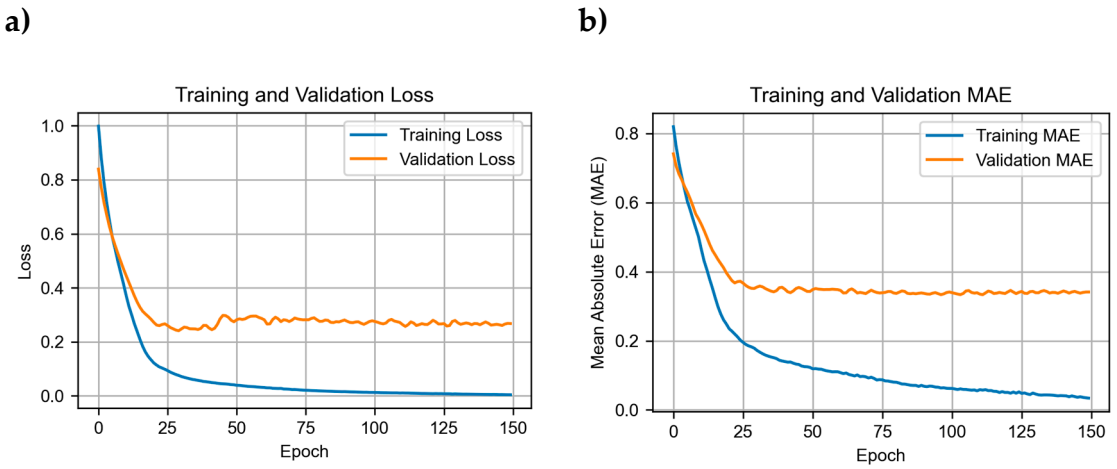

Figure 5. Training and validation of the symmetric neural network by means of: a) loss function and b) MAE.

The results presented in the Figure 6 show a direct comparison between the actual values and the predictions made by the model for the three critical output variables: bead area, heat affected zone (HAZ), and penetration. These graphs allow the model's predictive ability to be assessed based on its accuracy and fit to the actual data.

Figure 6a shows the prediction of the bead area, where the blue lines (actual values) and orange lines (predicted values) show a close fit in most cases. Although there are slight deviations at some points, the general trend between the predictions and the actual values is consistent, indicating that the model is able to capture the main variations of this characteristic. Figure 6b shows the results of the prediction of the heat affected zone (HAZ). In this case, the model also shows a remarkable ability to replicate the behavior of the actual data. The correspondence between the two curves is quite high, especially in areas with pronounced changes. This suggests that the model can adapt to abrupt and complex transitions in the data.

In subplot Figure 6c the results for penetration are presented. Here, the agreement between the actual and predicted values is visible, with slight discrepancies in some intervals. However, the model proves to be able to capture the general trend of the data, reflecting a solid performance in predicting this critical characteristic.

 doi:10.20944/preprints202501.0027.v1

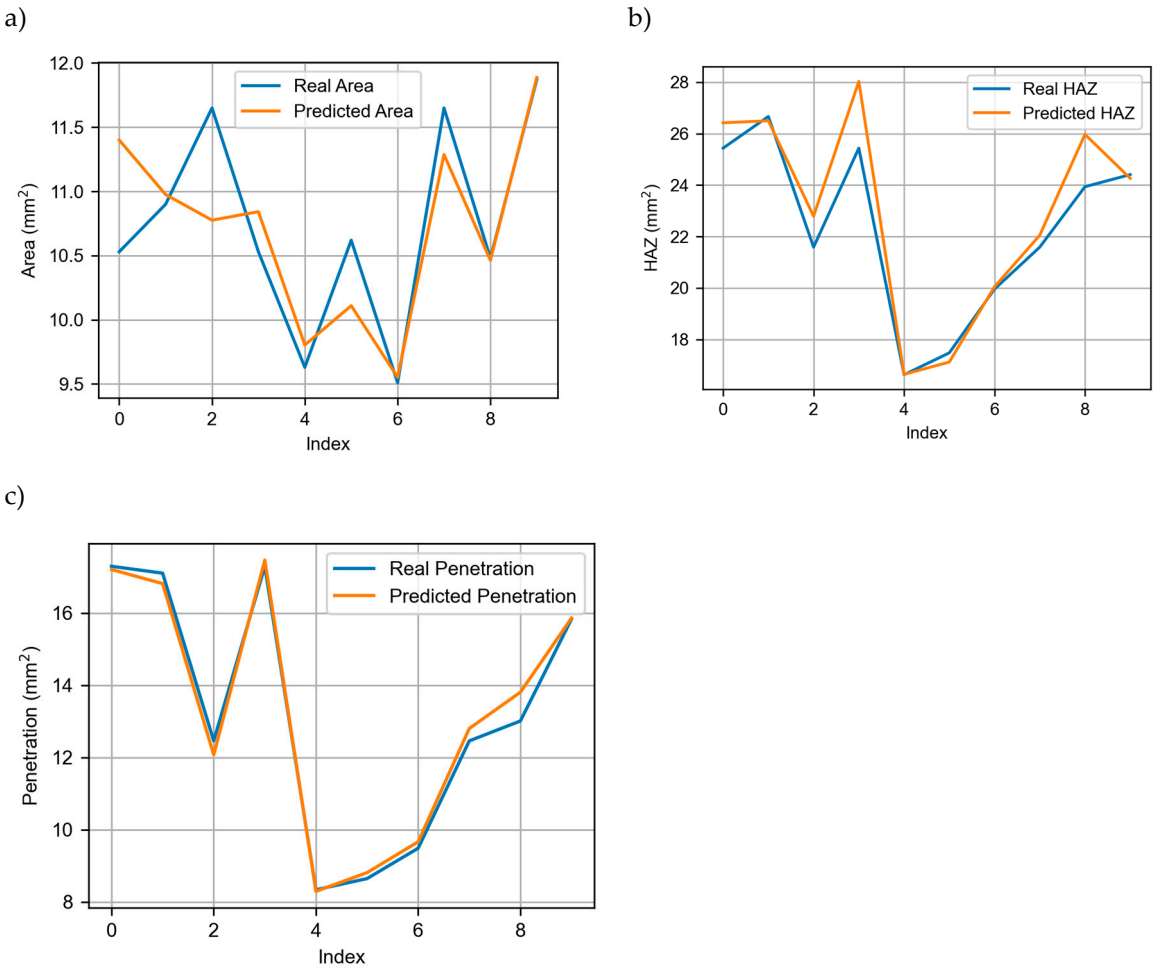

Figure 6. Prediction results versus actual values in the case of the critical output variables: a) Bead area, b) HAZ, and c) Penetration.

These results show that the designed neural network model can effectively predict the three critical output variables. Although not all predictions are accurate, the close fit and similar trends in predicted and actual values suggest that the model has a good ability to generalize the patterns present in the data. This behavior is key to its applicability in problems related to welding analysis and other similar applications.

4. Conclusions

In the present work, zero bead tests have been carried out using the GMAW (Gas Metal Arc Welding) welding process, using three types of substrates with different sheet thicknesses: 8 mm, 10 mm and 30 mm. During the welding process, key parameters such as feed rate and deposition rate have been varied, always keeping the amount of material deposited per meter advanced constant.

Throughout the experiments, a series of data has been collected, including the voltage and current of the welding generator. Subsequently, the main geometric indicators that characterize the weld bead have been extracted. This has allowed a detailed analysis of the influence of the welding parameters on the areas of the weld, providing a clearer view of how these affect the quality and characteristics of the bead.

Finally, we have developed a symmetric neural network capable of estimating the areas of the weld bead based on measurements from the heat source and the profilometer, which measures the visible geometry of the bead. This model has proven to be effective in predicting weld areas under controlled conditions.

 doi:10.20944/preprints202501.0027.v1

As for future lines, it is proposed to adapt this model for direct implementation in welding machines, so that it allows monitoring of the process in real time. In addition, it is sought to integrate this tool into the control loop of the welding process, which could contribute to a significant improvement in the quality of the weld and the optimization of process parameters in industrial applications.

Author Contributions: Conceptualization, F.V. and A.S.; data curation, A.F., V.U. and F.V.; formal analysis, A.F. and F.V.; investigation, F.V. and A.S.; methodology, A.F., V.U., X.S., and F.V.; project administration, A.S. and J-R.A.; supervision, J-R.A., A.S.; validation, V.U., J-R.A., A.S.; writing—original draft, A.F. and F.V.; writing—review and editing, A.F., J-R.A., X.S., and A.S. All authors have read and agreed to the published version of the manuscript.

Funding: This research was funded by the Spanish Ministry of Science and Innovation (MCIN/AEI/10.13039/501100011033) under the project FactorIA (grant number PLEC2024-011165) and supported as part of the ADDILANZA project by the Euroregion Nouvelle-Aquitaine Euskadi Navarra through the "Euroregional Innovation" program.

Institutional Review Board Statement: Not applicable

Informed Consent Statement: Not applicable

Data Availability Statement: The data presented in this study are available on request from the corresponding author.

Conflicts of Interest: The authors declare no conflict of interest.

References

1. Zhang, H.; Li, R.; Liu, J.; Wang, K.; Weijian, Q.; Shi, L.; Lei, L.; He, W.; Wu, S. State-of-Art Review on the Process-Structure-Properties-Performance Linkage in Wire Arc Additive Manufacturing. *Virtual and Physical Prototyping* **2024**, *19*, e2390495, doi:10.1080/17452759.2024.2390495.
2. He, F.; Yuan, L.; Mu, H.; Ros, M.; Ding, D.; Pan, Z.; Li, H. Research and Application of Artificial Intelligence Techniques for Wire Arc Additive Manufacturing: A State-of-the-Art Review. *Robotics and Computer-Integrated Manufacturing* **2023**, *82*, 102525, doi:10.1016/j.rcim.2023.102525.
3. Özel, T.; Shokri, H.; Loizeau, R. A Review on Wire-Fed Directed Energy Deposition Based Metal Additive Manufacturing. *JMMP* **2023**, *7*, 45, doi:10.3390/jmmp7010045.
4. Aldalur, E.; Veiga, F.; Suárez, A.; Bilbao, J.; Lamikiz, A. Analysis of the Wall Geometry with Different Strategies for High Deposition Wire Arc Additive Manufacturing Uraldeof Mild Steel. *Metals* **2020**, *10*, 892, doi:10.3390/met10070892.
5. Dinovitzer, M.; Chen, X.; Laliberte, J.; Huang, X.; Frei, H. Effect of Wire and Arc Additive Manufacturing (WAAM) Process Parameters on Bead Geometry and Microstructure. *Additive Manufacturing* **2019**, *26*, 138–146, doi:10.1016/j.addma.2018.12.013.
6. Zahidin, M.R.; Yusof, F.; Abdul Rashid, S.H.; Mansor, S.; Raja, S.; Jamaludin, M.F.; Manurung, Y.Hp.; Adenan, M.S.; Syahriah Hussein, N.I. Research Challenges, Quality Control and Monitoring Strategy for Wire Arc Additive Manufacturing. *Journal of Materials Research and Technology* **2023**, *24*, 2769–2794, doi:10.1016/j.jmrt.2023.03.200.
7. Xia, C.; Pan, Z.; Polden, J.; Li, H.; Xu, Y.; Chen, S.; Zhang, Y. A Review on Wire Arc Additive Manufacturing: Monitoring, Control and a Framework of Automated System. *Journal of Manufacturing Systems* **2020**, *57*, 31–45, doi:10.1016/j.jmsy.2020.08.008.
8. Wu, B.; Pan, Z.; Ding, D.; Cuiuri, D.; Li, H.; Xu, J.; Norrish, J. A Review of the Wire Arc Additive Manufacturing of Metals: Properties, Defects and Quality Improvement. *Journal of Manufacturing Processes* **2018**, *35*, 127–139, doi:10.1016/j.jmapro.2018.08.001.
9. Nguyen, V.-T.; Minh, P.S.; Uyen, T.M.T.; Do, T.T.; Ngoc, H.V.T.; Le, M.-T.; Tien Nguyen, V.T. WAAM Technique: Process Parameters Affecting the Mechanical Properties and Microstructures of Low-Carbon Steel. *Metals* **2023**, *13*, 873, doi:10.3390/met13050873.

 doi:10.20944/preprints202501.0027.v1

10. Kalashnikov, K.N.; Chumaevskii, A.V.; Kalashnikova, T.A.; Kolubaev, E.A. A Substrate Material and Thickness Influence on the 3D-Printing of Ti–6Al–4V Components via Wire-Feed Electron Beam Additive Manufacturing. *Journal of Materials Research and Technology* **2022**, *16*, 840–852, doi:10.1016/j.jmrt.2021.12.024.
11. Gupta, N.K.; Ganesan, G.; Siddhartha, S.; Karade, S.R.; Singh, S.D.; Karunakaran, K.P. A Dual-Side Deposition Technique to Mitigate Deformation in Wire Arc Additive Manufacturing. *Trans Indian Inst Met* **2024**, *77*, 3425–3434, doi:10.1007/s12666-024-03350-8.
12. Fang, X.; Zhang, L.; Yang, J.; Bai, H.; Zhao, L.; Huang, K.; Lu, B. Effect of Characteristic Substrate Parameters on the Deposition Geometry of CMT Additive Manufactured Al-6.3%Cu Alloy. *Applied Thermal Engineering* **2019**, *162*, 114302, doi:10.1016/j.applthermaleng.2019.114302.
13. Denkena, B.; Wichmann, M.; Böß, V.; Malek, T. Technological Simulation of the Resulting Bead Geometry in the WAAM Process Using a Machine Learning Model. *Procedia CIRP* **2024**, *126*, 627-627–632, doi:10.1016/j.procir.2024.08.269.
14. Xia, C.; Pan, Z.; Zhang, S.; Li, H.; Xu, Y.; Chen, S. Model-Free Adaptive Iterative Learning Control of Melt Pool Width in Wire Arc Additive Manufacturing. *Int J Adv Manuf Technol* **2020**, *110*, 2131–2142, doi:10.1007/s00170-020-05998-0.
15. Xia, C.; Pan, Z.; Zhang, S.; Polden, J.; Wang, L.; Li, H.; Xu, Y.; Chen, S. Model Predictive Control of Layer Width in Wire Arc Additive Manufacturing. *Journal of Manufacturing Processes* **2020**, *58*, 179–186, doi:10.1016/j.jmapro.2020.07.060.
16. Cambon, C.; Bendaoud, I.; Rouquette, S.; Soulié, F. A WAAM Benchmark: From Process Parameters to Thermal Effects on Weld Pool Shape, Microstructure and Residual Stresses. *Materials Today Communications* **2022**, *33*, 104235, doi:10.1016/j.mtcomm.2022.104235.
17. Aldalur, E.; Veiga, F.; Suárez, A.; Bilbao, J.; Lamikiz, A. High Deposition Wire Arc Additive Manufacturing of Mild Steel: Strategies and Heat Input Effect on Microstructure and Mechanical Properties. *Journal of Manufacturing Processes* **2020**, *58*, 615–626, doi:10.1016/j.jmapro.2020.08.060.
18. Wang, L.; Shen, C.; Zhang, Y.; Li, F.; Zhou, W.; Ruan, G.; Ding, Y.; Wu, K.; Hua, X. Investigation on Microstructure Characteristics and Mechanical Properties of Twin Wire-Directed Energy Deposition-Arc Fabricated TiAl Alloy Regulated by the Line Energy. *Intermetallics* **2024**, *165*, 108144, doi:10.1016/j.intermet.2023.108144.
19. Fang, X.; Zhang, L.; Chen, G.; Dang, X.; Huang, K.; Wang, L.; Lu, B. Correlations between Microstructure Characteristics and Mechanical Properties in 5183 Aluminium Alloy Fabricated by Wire-Arc Additive Manufacturing with Different Arc Modes. *Materials* **2018**, *11*, doi:10.3390/ma11112075.
20. Uralde, V.; Veiga, F.; Suarez, A.; Aldalur, E.; Ballesteros, T. Symmetry Analysis in Wire Arc Direct Energy Deposition for Overlapping and Oscillatory Strategies in Mild Steel. *Symmetry* **2023**, *15*, 1231, doi:10.3390/sym15061231.
21. Veiga, F.; Suárez, A.; Aldalur, E.; Bhujangrao, T. Effect of the Metal Transfer Mode on the Symmetry of Bead Geometry in WAAM Aluminum. *Symmetry* **2021**, *13*, 1245, doi:10.3390/sym13071245.
22. Uralde, V.; Veiga, F.; Aldalur, E.; Suarez, A.; Ballesteros, T. Symmetry and Its Application in Metal Additive Manufacturing (MAM). *Symmetry* **2022**, *14*, 1810, doi:10.3390/sym14091810.
23. Mattera, G.; Polden, J.; Norrish, J. Monitoring the Gas Metal Arc Additive Manufacturing Process Using Unsupervised Machine Learning. *Weld World* **2024**, *68*, 2853–2867, doi:10.1007/s40194-024-01836-z.
24. Karmuhilan, M.; Sood, A.K. Intelligent Process Model for Bead Geometry Prediction in WAAM. *Materials Today: Proceedings* **2018**, *5*, 24005–24013, doi:10.1016/j.matpr.2018.10.193.
25. Coutinho, F.; Lizarralde, N.; Mendes, M.; Bostrom, R.; Silva, T.; Couto, M.; Lizarralde, F. iWAAM: An Automated System for Monitoring and Control of Wire-Arc Additive Manufacturing. *IFAC-PapersOnLine* **2023**, *56*, 6576–6581, doi:10.1016/j.ifacol.2023.10.309.
26. Li, Y. Machine Learning Based Defect Detection in Robotic Wire Arc Additive Manufacturing. *University of Wollongong Thesis Collection 2017* **2021**.
27. Wang, J.; Zhao, B.; Liu, Y.; Zhao, J.; Ma, G. Research Progress in Shape-Control Methods for Wire-Arc-Directed Energy Deposition. *Materials* **2024**, *17*, 5704, doi:10.3390/ma17235704.

28. Cunningham, C.R.; Flynn, J.M.; Shokrani, A.; Dhokia, V.; Newman, S.T. Invited Review Article: Strategies and Processes for High Quality Wire Arc Additive Manufacturing. *Additive Manufacturing* **2018**, *22*, 672–686, doi:10.1016/j.addma.2018.06.020.
29. Min Seop So; Mohammad Mahruf Mahdi; Duck Bong Kim; Jong-Ho Shin Prediction of Metal Additively Manufactured Bead Geometry Using Deep Neural Network. *Sensors* **2024**, *24*, 6250-6250–6250, doi:10.3390/s24196250.
30. Uralde, V.; Veiga, F.; Suarez, A.; Lopez, A.; Goenaga, I.; Ballesteros, T. Novel Sensorized Additive Manufacturing-Based Enlighted Tooling Concepts for Aeronautical Parts. *Scientific Reports* 2024, *14*.
31. Fidan, I.; Huseynov, O.; Ali, M.A.; Alkunte, S.; Rajeshirke, M.; Gupta, A.; Hasanov, S.; Tantawi, K.; Yasa, E.; Yilmaz, O.; et al. Recent Inventions in Additive Manufacturing: Holistic Review. *Inventions* **2023**, *8*, 103, doi:10.3390/inventions8040103.